NANO · MICRO small
www.small-journal.com

Temperature-Feedback Nanoplatform for NIR-II Penta-Modal Imaging-Guided Synergistic Photothermal Therapy and CAR-NK Immunotherapy of Lung Cancer

*Mengze Xu, Bin Xue, Yue Wang, Dan Wang, Duyang Gao, Shuo Yang, Qi Zhao, Cangtao Zhou, Shuangchen Ruan, and Zhen Yuan**

In this study, to visually acquire all-round structural and functional information of lung cancer while performing synergistic photothermal therapy (PTT) and tumor-targeting immunotherapy, a theranostic nanoplatform that introduced upconversion nanoparticles (UCNPs) and IR-1048 dye into the lipid-aptamer nanostructrure (UCILA) is constructed. Interestingly, the IR-1048 dye grafted into the lipid bilayer can serve as the theranostic agent for photoacoustic imaging, optical coherence tomography angiography, photothermal imaging, and PTT in the second near infrared (NIR-II) window. In addition, loaded in the inner part of UCILA, UCNPs possess the superior luminescence property and high X-ray attenuation coefficient, which can act as contrast agents for computed tomography (CT) and thermo-sensitive up-conversion luminescence (UCL) imaging, enabling real-time tracking of metabolic activity of tumor and temperature-feedback PTT. Furthermore, under the complementary guidance of penta-modal imaging and an accurate monitoring of in situ temperature change during PTT, UCILA exhibits its excellent capability for ablating the lung tumor with minimal side effects. Meanwhile, synergistic CAR-NK immunotherapy is carried out specifically to eradicate any possible residual tumor cells after PTT. Therefore, the UCILA nanoplatform is demonstrated as a multifunctional theranostic agent for both penta-modal imaging and temperature-feedback PTT while conducting targeting immunotherapy of lung cancer.

1. Introduction

To date, lung cancer remains one of the leading causes of global mortality, causing about 1.8 million deaths in 2020.[1] In particular, the nonsmall cell lung cancer that is not always response to the majority of chemotherapeutic drugs, accounts for 85% of lung cancer with less than 15% of 5-year survival rate. In addition, surgical resection of the nonsmall cell lung cancer suffers from relapse or recurrence due to the poor prognosis and difficulties in determining cancer margin during surgery, making it easily metastasize to multiple sites of human body.[2] Further, radiotherapy is another effective way to treat the nonsmall cell lung cancer, which might cause significant side effects due to high dose radiation.[3–5] Therefore, to enhance the efficacy of nonsmall cell lung cancer therapy, tremendous efforts have been devoted to developing various theranostics methods, such as immunotherapy,[6] targeted therapy,[7] or phototherapy.[8] More specifically, photothermal therapy (PTT) has exhibited its superior advantages in cancer treatment including controllable therapeutic process and elevated eradication efficiency.[9–11]

However, the process of PTT could damage normal tissues when utilizing giant heat generated by photothermal agents to kill tumor cells. Therefore, temperature-feedback photothermal agents are essential for real-time sensing/monitoring the microscopic temperature changes during PTT.[12] More importantly, the constructed photothermal agent should exhibit its capability to completely destroy the tumor tissues

Dr. M. Xu, Dr. B. Xue, Dr. Y. Wang, Dr. D. Wang, Dr. D. Gao, Dr. S. Yang, Prof. Q. Zhao, Prof. Z. Yuan
Cancer Center
Faculty of Health Sciences
University of Macau
Macau SAR 999078, P. R. China
E-mail: zhenyuan@um.edu.mo
Dr. M. Xu, Prof. Z. Yuan
Centre for Cognitive and Brain Sciences
University of Macau
Macau SAR 999078, China
Dr. M. Xu, Prof. Z. Yuan
MoE Frontiers Science Center for Precision Oncology
University of Macau
Macau SAR 999078, China
Dr. B. Xue, Prof. C. Zhou, Prof. S. Ruan
Center for Advanced Material Diagnostic Technology
Shenzhen Key Laboratory of Ultraintense Laser and Advanced Material Technology
College of Engineering Physics
Shenzhen Technology University
Shenzhen 518118, P. R. China
The ORCID identification number(s) for the author(s) of this article can be found under https://doi.org/10.1002/smll.202101397.

DOI: 10.1002/smll.202101397

and concurrently protect the normal cells. Additionally, it is also extremely challenging for PTT to totally ablate large-volume tumors because of the residual tumor mass located along the treatment margins. By contrast, a synergistic therapeutic strategy that combines immunotherapy and PTT might be a promising therapeutic technique to improve the overall efficacy of tumor treatment. Besides, the multimodality molecular imaging-guided PTT based on tumor-targeting drug delivery systems is being developed into a representative cancer treatment methodology.[13–15] In particular, the complementary information from each individual imaging technique, such as fluorescence (FL) imaging, photoacoustic (PA) imaging, computed tomography (CT), optical coherence tomography (OCT), and photothermal imaging (PTI) can be fused together to monitor the therapeutic response of tumor during PTT.[16–18]

Hence, a novel theranostic nanoplatform was constructed, which incorporated upconversion nanoparticles (UCNPs) and IR-1048 dye (NIR-II, 1000–1700 nm) into the lipid-aptamer nanostructrure (UCILA) for enhanced lung cancer detection and treatment. Interestingly, the upconversion spectrum is superior sensitive to the UCNPs' ambient temperature. Therefore, UCNPs based on $NaLuF_4$:Yb/Er@$NaLuF_4$ can not only serve as a FL probe to dynamically monitor the temperature changes of PTT, but also as a contrast agent for CT and thermosensitive upconversion luminescence (UCL) imaging, enabling real-time trace of metabolic activity of lung cancer in vivo and temperature-feedback PTT.[19–23] In particular, the PA imaging, a novel noninvasive and nonionic biomedical imaging method, can be utilized to monitor the therapeutic response of photothermal therapy due to its much higher in vivo imaging depth than conventional optical imaging, and the optical-resolution photoacoustic microscopy (OR-PAM) possesses higher resolution and contrast than magnetic resonance imaging and CT.[24] Moreover, the OR-PAM and OCT could clearly capture the neovascularization of tumor, and it has been previously reported that photothermal agents often possessed photoacoustic imaging effect.[25] On the other hand, even though PT imaging by thermal imager could detect the lesion temperature under laser irradiation, the accuracy may be affected by the distance and air loss. To summarize mentioned above, taking the UCL, CT, OCT, PA imaging, and PTI together (namely penta-modal imaging) would be a complementary way to achieve accurate early-diagnosis, efficient in-process monitoring of the therapeutic response and final excellent efficacy of the precise PTT and immunotherapy with minimal side-effect.[26–30] In addition, the organic dye (IR-1048) component inside UCILA can also work as NIR-II agents for PTI, OCT imaging, PAI, and PTT, [31–33] which can capture, respectively, the tumor microenvironments and 3D tumor tissue changes (OCT), tumor blood oxygen and vasculature change (PAI) and tumor temperature changes (PTI) during depth -resolved NIR-II PTT.[34,35] Further, the aptamer namely AS1411 modified liposomes that encapsulate both IR-1048 dye and UCNPs, were able to improve the poor water-solubility of the organic dye IR-1048 and to concurrently achieve cancer-targeting theranostics by enhanced permeability and retention effect.[36–45]

Besides, another key issue that has to been addressed for the present work is that tumor-targeting PTT itself cannot completely ablate the whole solid tumors. Therefore, the residual cancer cells could easily enter the systemic blood vessels, inducing tumor metastasis and recurrence. By contrast, immunotherapy involving immune checkpoints like anti-PD-1 antibodies has been successfully carried out after PTT. In particular, natural killer (NK) cells, e.g., chimeric-antigen-receptor-modified natural killer (CAR-NK) cells, play an essential role in deterring cancer cells from metastasis although NK cells alone are incapable to totally eliminate the tumor cells because of immunosurveillance evasion.[46] Hence artificial receptor-decorated NK cells have been inspected to redirect immune cells against tumor cells, which are not able to evoke immune storm as compared to the chimeric antigen receptor (CAR) T-cell (CAR-T) therapy. More specifically, the immune checkpoint B7-H3 molecule exhibits a platonic target for lung cancer immunotherapy.[47–54] As such, CAR-NK cells carrying anti-B7-H3 as a supplementary therapy was performed for the present work after PTT to directional remove the residual cancer cells. It is expected that CAR can activate the NK cells to recognize, specifically target and inhibit the nonsmall cell lung cancer vasculature in which B7-H3 receptor is overexpressed, preventing tumor immune escape.

Consequently, in this study, we illustrated a facile nanoengineering method that endow UCILA with a number of superior performances to thoroughly remove lung cancer by tumor-targeting and temperature-feedback NIR-II PTT as well as tumor-targeting CAR-NK immunotherapy (**Scheme 1**). Meanwhile, UCILA also serve as the contrast agent for NIR-II five-modal optical molecular imaging, offering all-round structural and functional information for precise measurements of therapeutic responses in microenvironment of lung cancer to enhance the anticancer efficacy.[55–57] After temperature-feedback PTT, the tumors in the living mice were almost ablated without over-heat to the circumambient normal tissue. And only the PTT and CAR-NK cotreated group mice showed no relapse and no metastasis and well recovered in comparison to other groups. Therefore, due to the complementary guidance of penta-modal imaging, UCILA can be a superior candidate to eradicate the nonsmall-cell lung carcinoma with minimal side-effects.

2. Results and Discussion

2.1. Synthesis and Characterization of UCILA

UCILA was successively prepared through several steps. As the inner part, the as-designed UCNPs ($NaLuF_4$:Yb/Er@$NaLuF_4$ core–shell nanoparticles) were synthesized via the solvothermal method.[54,55] Transmission electron microscopy (TEM) micrograph revealed their nearly monodisperse particle size of about 18.5 ± 1.2 nm (**Figure 1**A). In addition, as illustrated by the high-resolution TEM (HRTEM) (Figure 1B) and the powder X-ray diffraction pattern (XRD) (Figure 1C), the as-synthesized UCNPs exhibited highly crystalline hexagonal phase. In particular, compare to the core nanoparticles (≈16 ± 1.1 nm, Figure S1A,B, Supporting Information), an optically inert shell layer of $NaLuF_4$ was epitaxially grown which enhanced the UCL (Figure S1C, Supporting Information). Further, the energy-dispersive X-ray spectroscopy demonstrated that the element of Lu was successfully doped in the UCNPs (Figure S1D, Supporting Information). On the other hand, as another coassembled part, DSPE-PEG_{2k}-AS1411 (abbr. DPA) was prepared through click

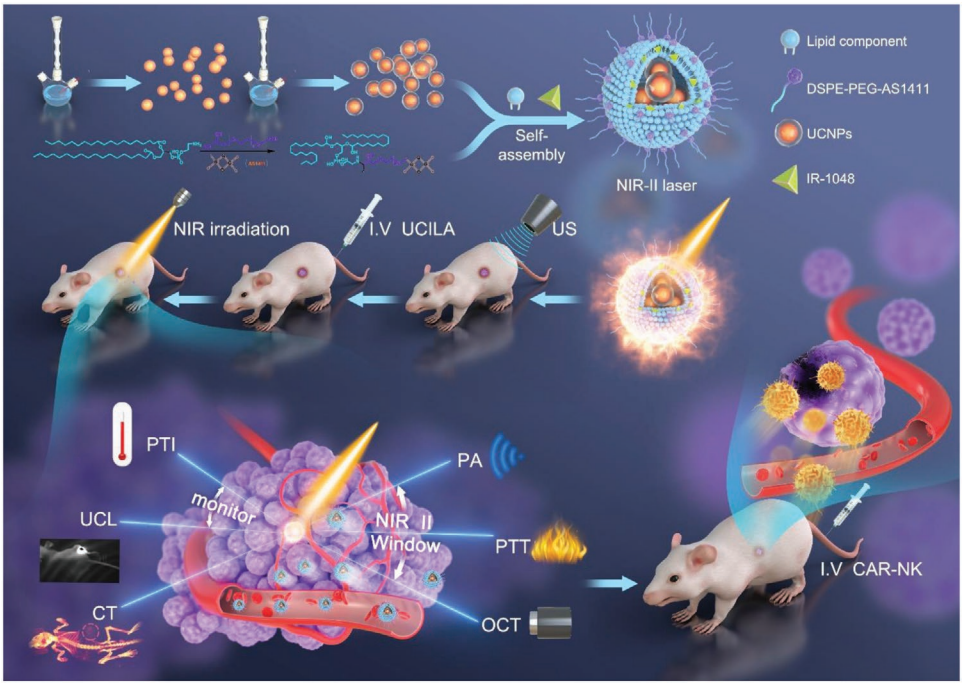

Scheme 1. Schematic illustration of NIR-II penta-modal imaging guided tumor-targeting precise photothermal therapy (PTT) and CAR-NK immunotherapy based on temperature-feedback UCILA nanoplatform. Penta-modal imaging consists of photoacoustic (PA) imaging, computed tomography (CT), thermal imaging (PTI), optical coherence tomography (OCT) angiography, and thermo-sensitive upconversion luminescence (UCL) imaging. US: Ultrasound.

chemistry between the thiolated group of 5'-SH-AS1411 aptamer and the maleimide group at the ends of the DSPE-PEG_{2k}-mal, whose conjugation of AS1411 aptamer with PEGylated DSPE was confirmed by MALDI-TOF mass spectrometry (Figure S1E, Supporting Information), in which the molecular weight varied from 8469.48 of AS1411 to around 11 410.62 of DPA after reaction with DSPE-PEG_{2k}-MAL. Then, the UCNPs, IR-1048, lipid components, and DPA was self-assembled to the final nanostrucrure of UCILA, whose uniform spherical morphology containing inner part of UCNPs and stained lipid layer was displayed in Figure 1D.

Besides, Fourier transform infrared (FT-IR) spectroscopy analysis was conducted, indicating that that the UCILA contained these parts (Figure 1E). Specifically, the FT-IR spectra of UCILA showed the characteristic peaks of ligand-free UCNPs (broad peak at 3435 cm^{-1} was attributed to the —OH vibration), IR-1048 (784, 1543, 1610, and 1638 cm^{-1}), whereas the stretching bands at 1096 and 1709 cm^{-1} denoted the amide bond of aptamer-modified lipid (DSPE-PEG-AS141). By contrast, the absorbance peak at 1071 nm (Figure 1F) was mainly due to the IR-1048, while the absorbance peak at 256 nm correlated with AS1411 aptamer was detected in UCILA spectrum (Figure S1F, Supporting Information). Moreover, gradually increased dynamic light scattering (DLS) sizes (Figure 1G) and variable zeta potentials (Figure 1H) further verified that the UCILA around 101.2 ± 7.1 nm and −24.27 ± 4.7 mV was successfully prepared. Likewise, the UCILA completely preserved the NIR absorption ability of IR-1048 in the NIR-II window (Figure 1F), which also presented the characteristic upconversion emission (green emission ($^2H_{11/2}/^4S_{13/2}\rightarrow{}^4I_{15/2}$, 520/540 nm) and red emission ($^4F_{9/2}\rightarrow{}^4I_{15/2}$, 650 nm)) of UCNPs (Figure 1I) and showed visible bright fluorescence upon the irradiation of 980 nm laser (Figure S2A, Supporting Information). More importantly, upon the NIR 980 nm excitation, UCILA also displayed nonlinear classic power-dependent UCL (Figure S2B–E, Supporting Information), which further demonstrated UCILA indeed own the UCL properties of UCNPs. It is also noted that PEG modified UCILA exhibited an excellent stability either in the p buffered saline (PBS) or in the physiological medium for 72 h without obvious change in particle diameters, homogeneity of solutions or absorbance (Figure S3A–F, Supporting Information).

2.2. NIR-II Photothermal Properties and In Vitro Penta-Modal Imaging Abilities of UCILA

To characterize the photothermal properties of UCILA, five groups of UCILA solutions with different concentrations (pure water served as the control group) were tested to inspect the temperature changes with 1064 nm laser irradiation at different power densities (0.25, 0.5, and 1.0 W cm^{-2}) for 6 min. As shown in **Figure 2**A, UCILA showed magnificent NIR-II laser power dependent effect. In addition, Figure 2B demonstrated that the temperature increased rapidly with increased concentrations of UCILA, in which the temperature increase can be up to 45.5 °C as compared to 7.1 °C of pure water. And the NIR-II thermal images in Figure 2C further illustrated concentration-dependent photothermal effect (laser power density: 1 W cm^{-2}). In particular, UCILA with a concentration of 42.75 μg mL^{-1} exhibited the largest temperature elevation upon 1 W cm^{-2} laser irradiation, which was then applied to the present in vitro and in vivo PTT. To examine the photothermal stability of UCILA, five laser on/off cycles upon the 1 W cm^{-2} irradiation of 1064 nm laser (Figure 2D) was carried out, and

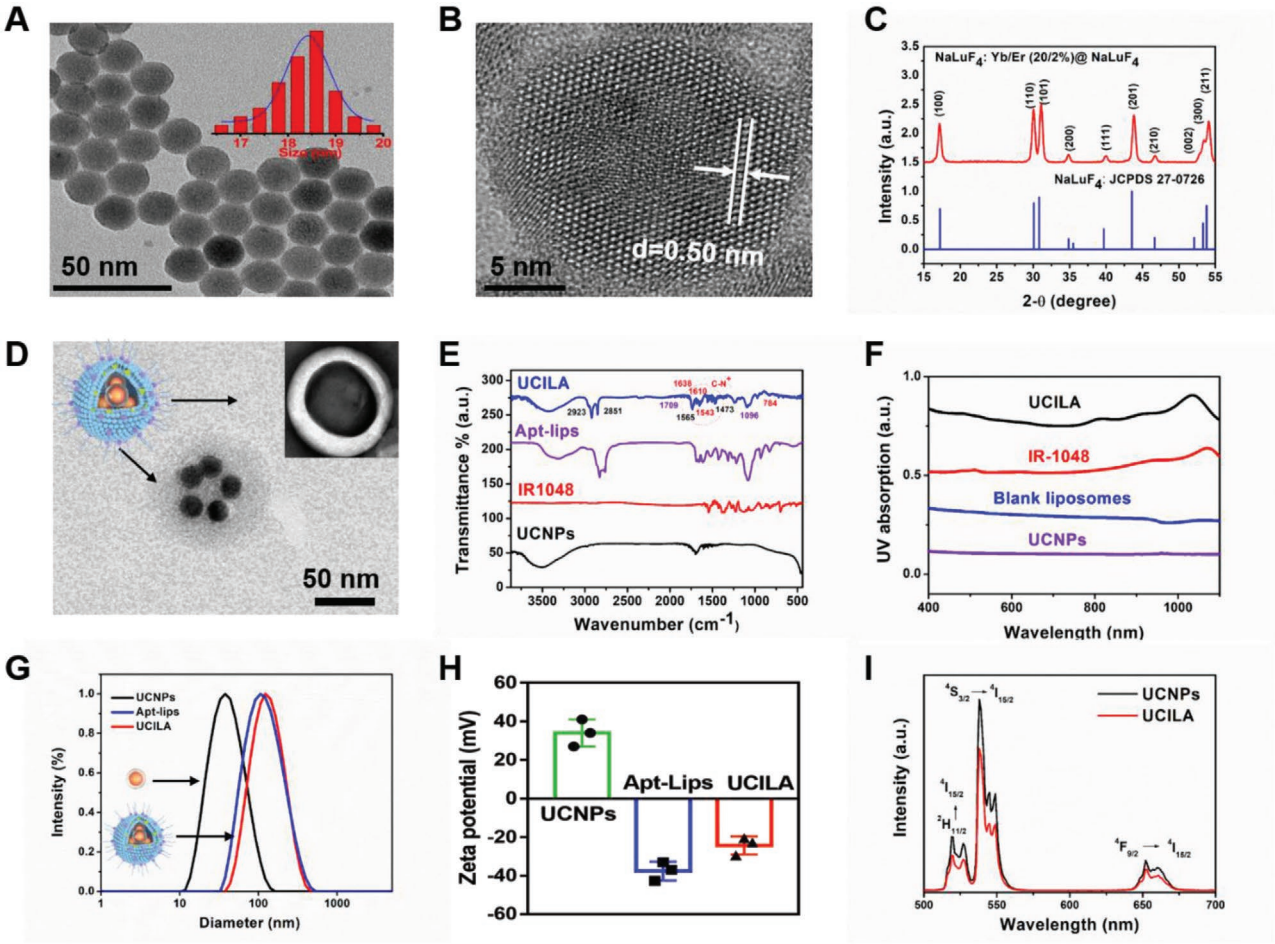

Figure 1. Physicochemical characterization of UCILA. A) TEM image of $NaLuF_4$:Yb/Er@$NaLuF_4$ core–shell nanoparticles and their size distribution. B) HRTEM image of the as-prepared UCNPs. C) XRD pattern of $NaLuF_4$:Yb/Er@$NaLuF_4$ core-shell nanoparticles (red line) and the standard line pattern of β-$NaLuF_4$ (blue line). D) TEM images of UCILA with inner image of UCILA after negative staining with phosphotungstic acid. E) FT-IR spectra of UCILA, aptamer-modified lipids (Apt-lips), IR-1048, and UCNPs. F) Absorption of UCILA, IR-1048, UCNPs, and blank liposomes contain apt-lips. G) DLS measurements of UCILA, UCNPs, and blank liposomes contain apt-lips. H) Zeta potentials of UCILA, UCNPs, and blank liposomes contain apt-lips. I) Fluorescence spectra of UCILA and UCNPs.

it almost reached to close highest and lowest temperature with similar temperature increasing and decreasing process, which showed excellent photostability. Then the UCILA's temperature evolution was recorded over time according to reversible heating-cooling cycles (Figure S4A, Supporting Information) while the photothermal conversion coefficient of UCILA was calculated to be 31.3% (Figure S4, Supporting Information), which is comparable to most organic and inorganic PTT agents.[58]

Besides the PTI for monitoring the macroscopic temperature of tumor site, the thermo-sensitive UCL can monitor the microscopic temperature change of UCILA. Since $^2H_{11/2}\rightarrow{}^4I_{15/2}$ (525 nm) and $^2S_{3/2}\rightarrow{}^4I_{15/2}$ transitions of Er^{3+} satisfy the following equation[55]

$$(I_{525})/(I_{545}) = C_1 \exp(-\Delta E/k_B T) \quad (1)$$

in which C is a constant determined by degeneracy, ΔE is the energy gap separating the two excited states, k_B is the Boltzmann constant, and T is temperature using the Kelvin scale. In addition, for the same UCNPs under the same excitation power densities, I_{545} was proportional to I_{655}, namely

$$I_{545} = C_2 I_{655} \quad (2)$$

$$(I_{525})/(I_{655}) = C_1 C_2 \exp(-\Delta E/k_B T) \quad (3)$$

Thus, I_{525}/I_{655} will be increased with the temperature and the dependence of ln $(I_{525})/(I_{655})$ on the inverse of temperature (1/T) follow a linear relationship. Experimentally, we indeed observed the linear relationship in Figure 2E according to the UCL spectra of UCILA at different temperatures (Figure 2F). The linear relationship could be fitted as ln $(I_{525})/(I_{655})$ = 2.8933–776.5 × (1/T) (T given in K). The relative sensitivity (S_r) of a thermometer is defined as[59,60]

$$S_r = (1/R) \times (dR/dT) \quad (4)$$

where R is luminescence ratio of the thermometer. Here, S_r was determined to be determined to be between 0.62% and

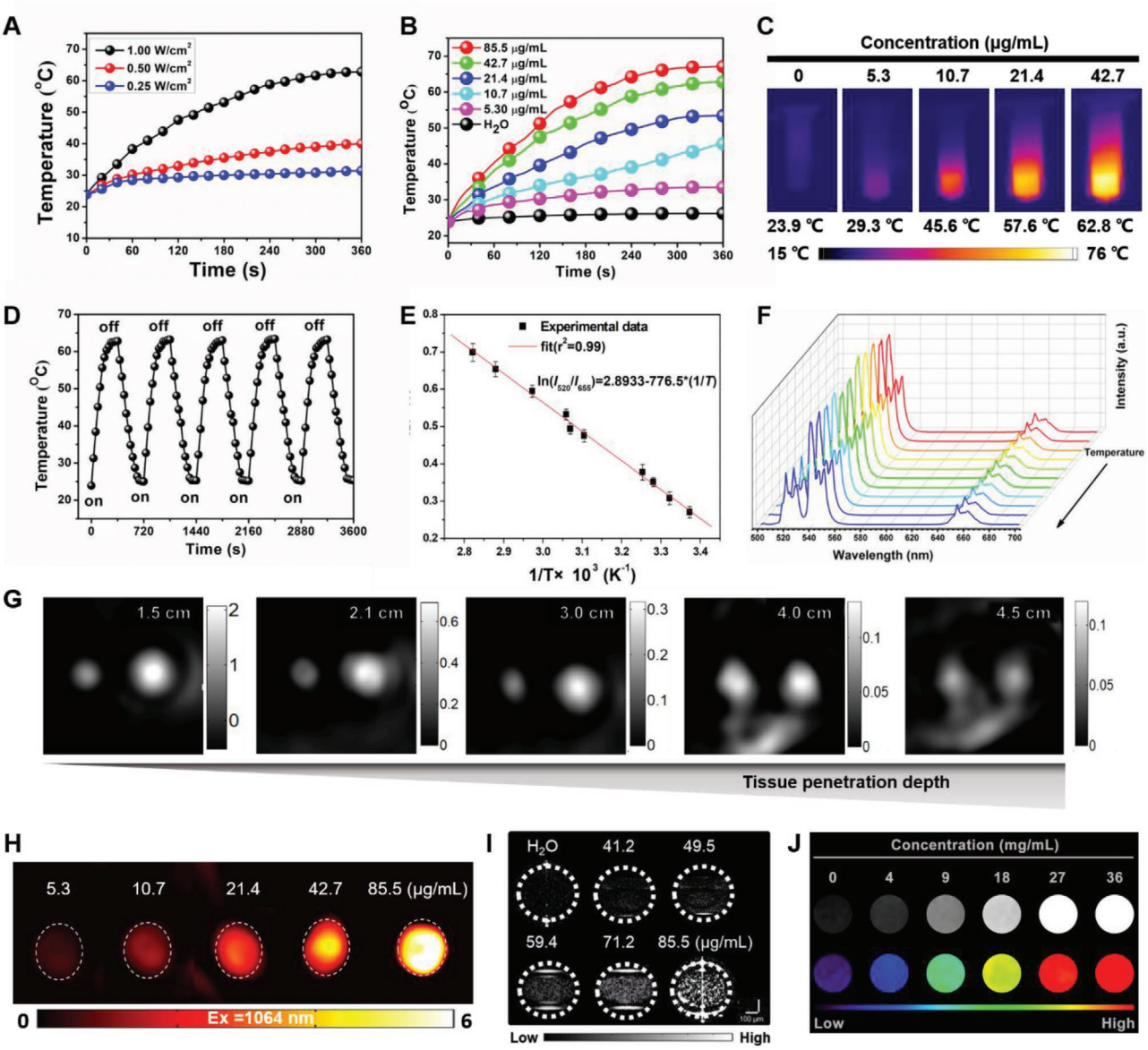

Figure 2. In vitro photothermal properties and multimodal imaging abilities of UCILA. A) Temperature curves of UCILA upon different 1064 nm laser density (0.25, 0.5, and 1 W cm^{-2}). B) Temperature raises of different concentrations of UCILA (IR-1048 concentration: 0, 5.3, 10.7, 21.4, 42.7, and 85.5 μg mL^{-1}) upon 1064 nm laser irradiation. C) Thermal imaging of UCILA solution at different concentration (0, 5.3, 10.7, 21.4, and 42.7 μg mL^{-1}) upon 1064 nm laser irradiation for 6 min. D) Temperature elevation of UCILA solutions through five laser on/off cycles. E) A plot of ln (I_{520}/I_{655}) versus 1/T to calibrate the thermometric scale for UCILA. I_{520} and I_{655} indicate the intensities of UCNPs emission of the $^2H_{11/2}\rightarrow{}^4I_{15/2}$ and $^4F_{9/2}\rightarrow{}^4I_{15/2}$ transitions, respectively. F) UCL spectra of UCILA at different temperatures (from 20 to 80 °C) by external heating. The peaks were normalized at 655 nm. *All scale bars of the reconstruction images range are 4 × 4 mm^2. G) PA intensity evolution with various thickness of chicken breast tissue slices under 1064 nm laser excitation. H) In vitro photoacoustic imaging tested by phantom assay with various concentration of IR-1048 in UCILA. I) Ex vivo OCT signal vs concentration. J) CT imaging ability test of UCILA.

0.9% K^{-1} in the 20–80 °C temperature range. The S_r value is among the highest reported in the literature for rare earth thermometers, as shown in **Table 1**.

Therefore, the UCL is able to detect the temperature changes during PTT process. Especially, the 525 nm emission and the 655 nm emissions are not close, so recording the fluorescence signal at 525 and 655 nm is favorable to imaging in vivo. By monitoring the microscopic temperature of UCILA with UCL combined with monitoring the macroscopic temperature of UCILA with PTI, it is promising to realize precise PTT to achieve better therapeutic effect, while preventing the overheat from damaging the ambient normal tissue and cells.[64,66,67]

However, only performing temperature monitoring by PTI and UCL imaging was insufficient to visualize other therapeutic response in tumor microenvironments like neovascularization variation and metabolic situation of the nanoplatforms. As such, NIR-II PA and NIR-II OCT as well as CT molecular imaging were also carried out to guide the cancer treatment by using UCILA as the theranostic agents.

Table 1. Comparison of the relative thermal sensitivities among several typical rare earth based optical thermometers.

System	Wavelength [nm]	S_r max [% K^{-1}]	Ref.
$NaLuF_4$:Yb/Er	520/655	0.9 (293 K)	This work
BiVO4:Yb/Er	552/658	0.84 (780 K)	[61]
$NaYF_4$:Yb/Er	525/545	1.2 (300 K)	[62]
$LiLaP_4O_{12}$:Yb/Tm/Eu	475/650	1.9 (193 K)	[63]
LaF_3:Nd	865/885	0.26 (305 K)	[64]
SrF_2: Yb/Tm/Eu	585/590	1.1 (298 K)	[65]

For investigation to the in vitro photoacoustic effect and tumor-tissue imaging depth of UCILA, our home-made photoacoustic tomography system was used to conduct the phantom assay and imaging depth assay by chicken breast tissues. As shown in Figure S5A (Supporting Information), UCILA exhibited strong photoacoustic absorption in NIR-II biological window and penetration depth for target-containing UCILA can be up to 4.5 cm (Figure 2G). And PA images of the phantoms containing a gradient of concentrations of UCILA showed linear relationship in Figure S5B (Supporting Information) and presented concentration-dependent raise of PA signals (Figure 2H), suggesting that UCILA own commendable PAI properties to track down its metabolic situation. Interestingly, we have observed that the solution of UCILA could also enhance the dynamic scattering signals of NIR-II OCT (Figure 2I) and found their linearity between the OCT signal and concentration of UCILA at the ex vivo level in Figure S5C (Supporting Information), which is an important functional method to assess tumor microvasculature changes. In addition, a gradient of concentrations of UCILA based on the concentrations of UCNPs were scanned to detect its CT imaging intensity. Figure 2J demonstrated that UCILA exhibited enhanced CT imaging capability by a concentration dependent way and the CT signal showed a linear relationship with the concentration of UCNPs (Figure S5D, Supporting Information). Therefore, UCILA were proved to be powerful contrast agents for penta-modal molecular imaging.

2.3. Cellular Uptake and In Vitro Photothermal Cytotoxicity of UCILA

To inspect the in vitro cellular uptake of UCILA, flow cytometry was carried out when A549 lung cancer cells were incubated with UCILA at various time points. It was discovered

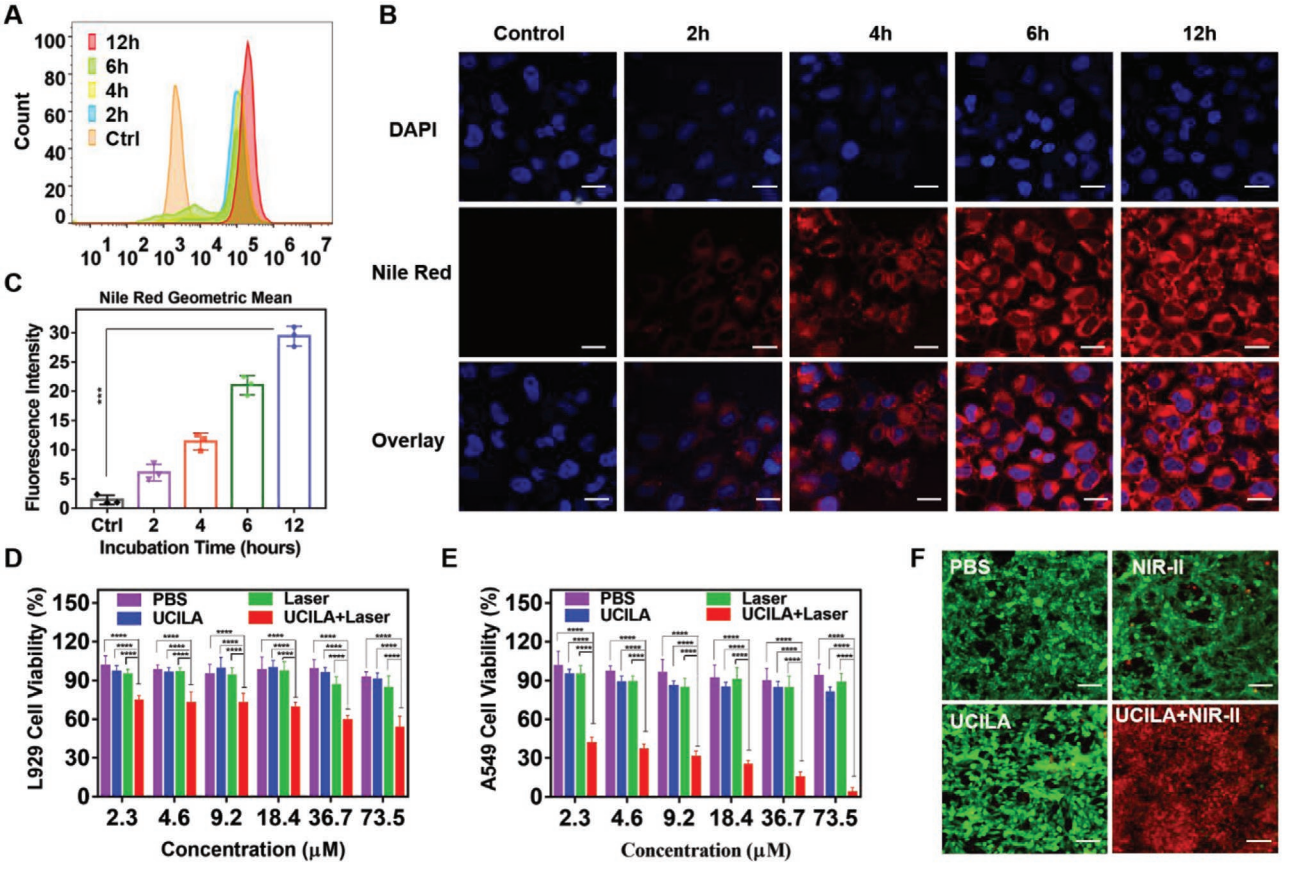

Figure 3. Cellular uptake and in vitro photothermal cytotoxicity. A) Flow cytometric analysis of A549 cells incubated with UCILA for 2, 4, 6, and 12 h, separately. B) Confocal images of A549 cells after 2, 4, 6, and 12 h incubation with UCILA, respectively. The UCILA were stained with Nile red, while the A549 cell nuclei were stained with DAPI. C) Quantitative analysis of the fluorescence intensity of uptaked UCILA stained by nile red at various incubation time. Relative D) L929 and E) A549 cell viability after treatments with various concentrations of UCILA after 1064 nm laser irradiation for 6 min or not. F) Fluorescence images of A549 cells after various treatments that were double-stained by Calcein-AM/PI. (Scale bar represents 100 μm). (mean ± SD; $n = 3$; $^*p < 0.05$, $^{**}p < 0.01$, $^{***}p < 0.001$, $^{****}p < 0.0001$).

from **Figure 3**A; and Figure S6A (Supporting Information) that the A549 cells uptake of UCILA was mostly detected at 12 h postcoincubation. And the laser scanning confocal images in Figure 3B (the overlay images of 4′,6-diamidino-2-phenylindole (DAPI) labeled nucleus of A549 cell and Nile Red labeled UCILA) exhibited the highest fluorescence intensity after 12 h coincubation, which further confirmed the flow cytometry analysis results. The quantitative analysis of the mean fluorescence intensity of uptaked UCILA stained by nile red at various incubation time were provided in Figure 3C. In particular, to explore the AS1411 aptamer-mediated tumor-targeting capability of UCILA, the A549 cancer cells were incubated with AS1411-modified UCILA and UCIL without AS1411, respectively. Simultaneously, L929 fibroblast was incubated with AS1411-modified UCILA. It turned out from Figure S6B,C (Supporting Information) that the A549 cancer cells uptake much higher concentrations of AS1411-modified UCILA than the UCIL without AS1411, and the Z-stack confocal slices of the dual stained cells were displayed in Figure S7 (Supporting Information). Whereas even though incubated with AS1411-modified UCILA, the L929 normal cells barely uptake the UCILA, demonstrating that UCILA can specifically target to the A549 cancer cells.

Furthermore, the cytotoxicity of UCILA was successfully assessed by examining the cell viability of both L929 fibroblast and A549 lung cancer cell lines when cultured in UCILA with various concentrations (from 2.3×10^{-6} M to 73.5×10^{-6} M) based on the standard CCK-8 assay at 24 h. In particular, the cell viabilities were also carefully inspected when the two categories of cells were treated according to four different ways: PBS alone, NIR-II laser alone, UCILA alone, and UCILA plus NIR-II laser irradiation.

It was discovered from Figure 3D,E that the cell viabilities of L929 fibroblast and A549 cells showed no detectable changes for all tested concentration cases without laser irradiation. However, this is not the case for the NIR-II laser irradiation treatment group, in which 47% L929 fibroblast and over 90% A549 cells were dramatically damaged in a concentrations-dependent way after incubation with UCILA. In particular, only UCILA plus Laser-treated group exhibited red fluorescence for A549 dead cells, while the other three treatment groups only show strong green fluorescence for live A549 cells, demonstrating the significant photothermal effect of UCILA (Figure 3F). The in vitro test results also demonstrated that UCILA owned excellent biocompatibility, high uptake property by A549 lung cancer cells, and high photothermal effect for destroying A549 cells. By contrast, UCILA showed much less photothermal cytotoxicity to the L929 normal cells (Figure 3D). The reason is because the A549 tumor cells that overexpressed nucleolin within the nucleus and along the surface of tumor cell membranes, exhibited much higher uptake of UCILA through binding to the AS1411 conjugated to it, whereas the L929 normal cells hardly express the receptor of AS1411, namely, nucleolin.[29]

2.4. Penta-Modal Imaging Guided Synergistic PTT and CAR-NK Immunotherapy of Lung Cancer

Encouraged by the excellent in vitro penta-modal imaging performance and efficient photothermal effect with high sensitivity to the temperature of UCILA, we then established the A549 tumor-bearing mice model to explore its in vivo imaging directed anticancer efficacy.

In vivo NIR-II PAI was first carried out by using our homemade PA tomography imaging system[14] and the recovered PA images before (pre) and after tail-vein injection of UCILA at various time points (2, 4, 6, 12 h) were plotted in **Figure 4**A. Interestingly, enhanced PA contrast at tumor site was clearly identified at 2 h postinjection of UCILA. And the PA signals gradually increased with increased time, which reached the peak at 4 h postinjection and began to decrease at 12 h postinjeciton. Therefore, UCILA were able to target and accumulate in the tumor, and then be metabolized from the mice. More importantly, since enhanced NIR-II PAI is able to promote the tumor neovasculature visualization (Figure S8A, Supporting Information), ultrasound (US) pretreatment immediately followed by tail-veil injection of UCILA is helpful to improve UCILA delivery efficiency into the solid tumor by ultrasound-assisted lymphatic drainage leaking into the tumor parenchyma.[68–71]

Besides, 3D whole-body CT imaging of A549 tumor xenografts-bearing nude mice (Figure 4B) was conducted, which can capture the metabolic process and accumulation of UCILA systemically inside the animal body. Again, it was discovered that CT imaging contrast of tumor was significantly enhanced for different time points after the tail-vein injection of UCILA as compared to that of before the injection (pre). In addition, CT imaging signal intensity gradually increased till reached the peak at 4 h postinjection and then began to decrease at 8 h postinjection (Figure S8B, Supporting Information).

Further, NIR-II PTI and thermo-sensitive UCL imaging were performed for imaging-guided and temperature-feedback NIR-II PTT of lung tumor in vivo. The first-round PTT was first carried out for 6 min, during which the temperature changes of tumor site were successfully mapped by the Fluke thermal imager (**Figure 5**A; and Figure S8C, Supporting Information). It was discovered that the tumor site exhibited almost no temperature change for the PBS treatment group. However, the temperature of UCILA treatment group was gradually increased up to 54.8 °C (Figure 5B).

Besides PTI was developed to track the temperature changes during PTT, as a proof of concept, we established a homemade system to monitor the UCL signal change of UCILA before and after PTT (Figure 5C). The ratio of I_{520}/I_{670} as shown (Figure S8D, Supporting Information) was indeed increased the increased temperature which was agreement with the theoretical estimate above. More accurately, the temperature calculated from the UCL spectra according to the fitted equation above, we found that the temperature as calculated from UCL spectra was higher than that of the PTI results (Figure 5C). We infer that this difference arose from that fluorescent imaging provided a local subtissue temperature measurement, whereas photothermal thermometry provided skin temperature.[64,66,67] Surface temperature will be lower than the subtissue location due to the heat diffusion process. Therefore, fluorescence imaging to monitor PTT temperature seems to be a better choice than PTI.

More importantly, to inspect the tumor vascular structures and tumor microenvironment changes before and

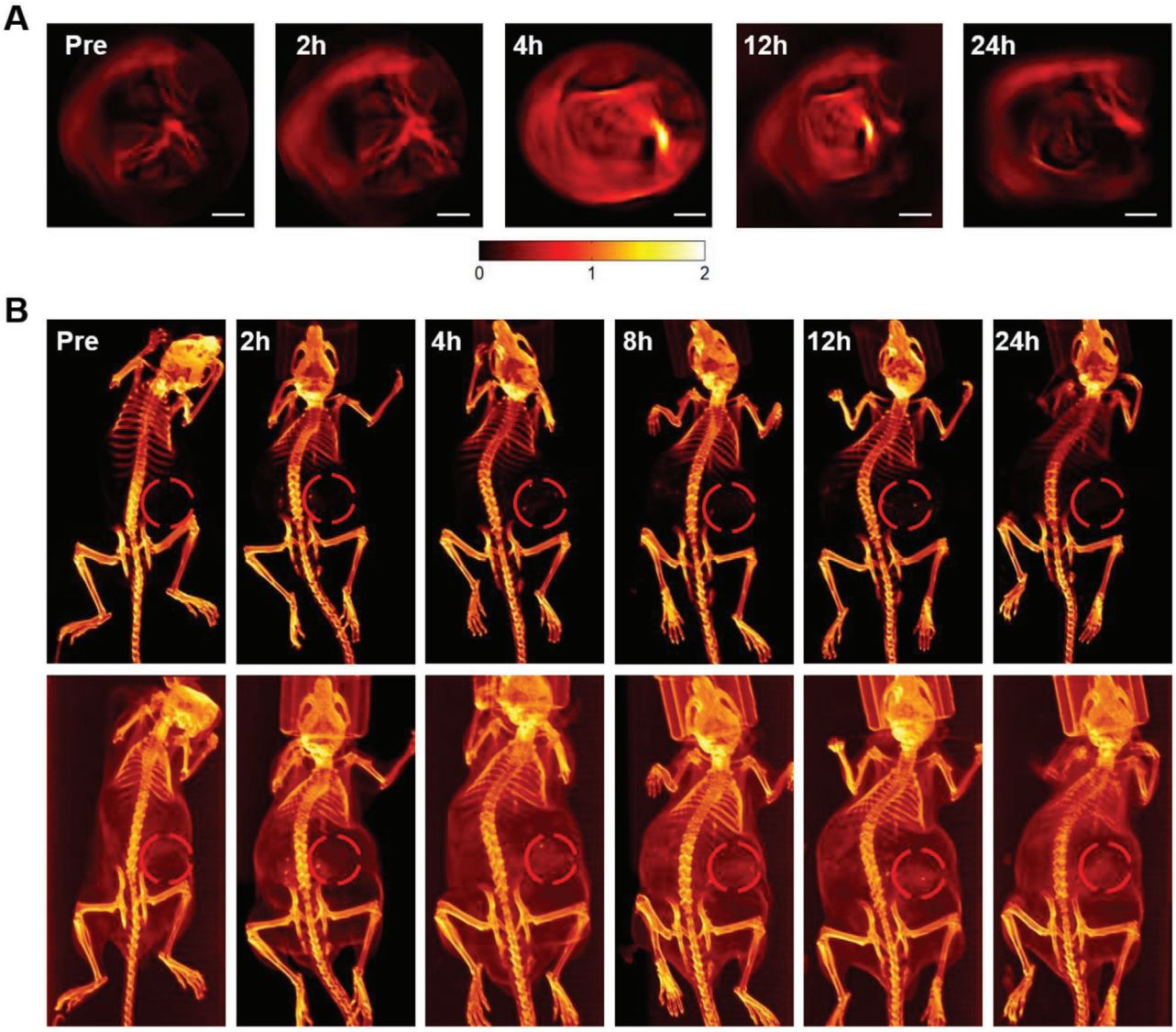

Figure 4. In vivo assessment of tumor microvasculature using photoacoustic (PA) imaging and OCT angiography. A) In vivo PA imaging of tumor vessels before and after tail-vein injection of UCILA under 1064 nm laser irradiation at different time points post tail-vein injected UCILA. *All scale bars of the reconstruction images range are 4×4 mm^2. B) In vivo CT images of A549 tumor-bearing mice at various time points after tail-vein injection of UCILA, which were displayed in two different ways.

after synergistic PTT and CAR-NK immunotherapy, NIR-II OCT imaging was carried out for the longitudinal follow-up of lung tumor angiography. For each measurement, we performed the tail-veil injection of the UCILA to conduct the OCT imaging. As shown in Figure 5E, the mice tumor microenvironment exhibited low-contrast structural and functional information of microvascular in 2D and 3D before tail-vein injection of UCILA. However, it was discovered from Figure 5E that NIR-II OCT imaging contrast was significantly enhanced in 2D and 3D postinjection of UCILA. More importantly, gradually decreased mean tumor blood vessel densities during the precise PTT and CAR-NK immunotherapy were visualized clearly. Therefore, UCILA were demonstrated that they can serve as the excellent NIR-II contrast agents for OCT imaging.

2.4.1. Synergistic PTT and CAR-NK Immunotherapy of Lung Cancer

To assess the efficacy of synergistic PTT and CAR-NK immunotherapy by using UCILA (**Figure 6**), the images and quantitative analysis of A549 tumor-bearing mice were acquired every 3 days with five different treatment groups: i) control group: PBS, ii) UCILA alone, iii) PBS with laser, iv) UCILA with laser, and v) UCILA with NIR-II laser irradiation followed by CAR-NK treatment.

Figure 6A schematically illustrated the inoculation of A549 tumor cells, NIR-II PTT and CAR-NK cells further enhancing the NIR-II PTT procedures. The flow cytometric analysis of CAR-NK-92MI cells demonstrated the successful CD56 and CAR expression on B7-H3-specific CAR-NK-92MI cells

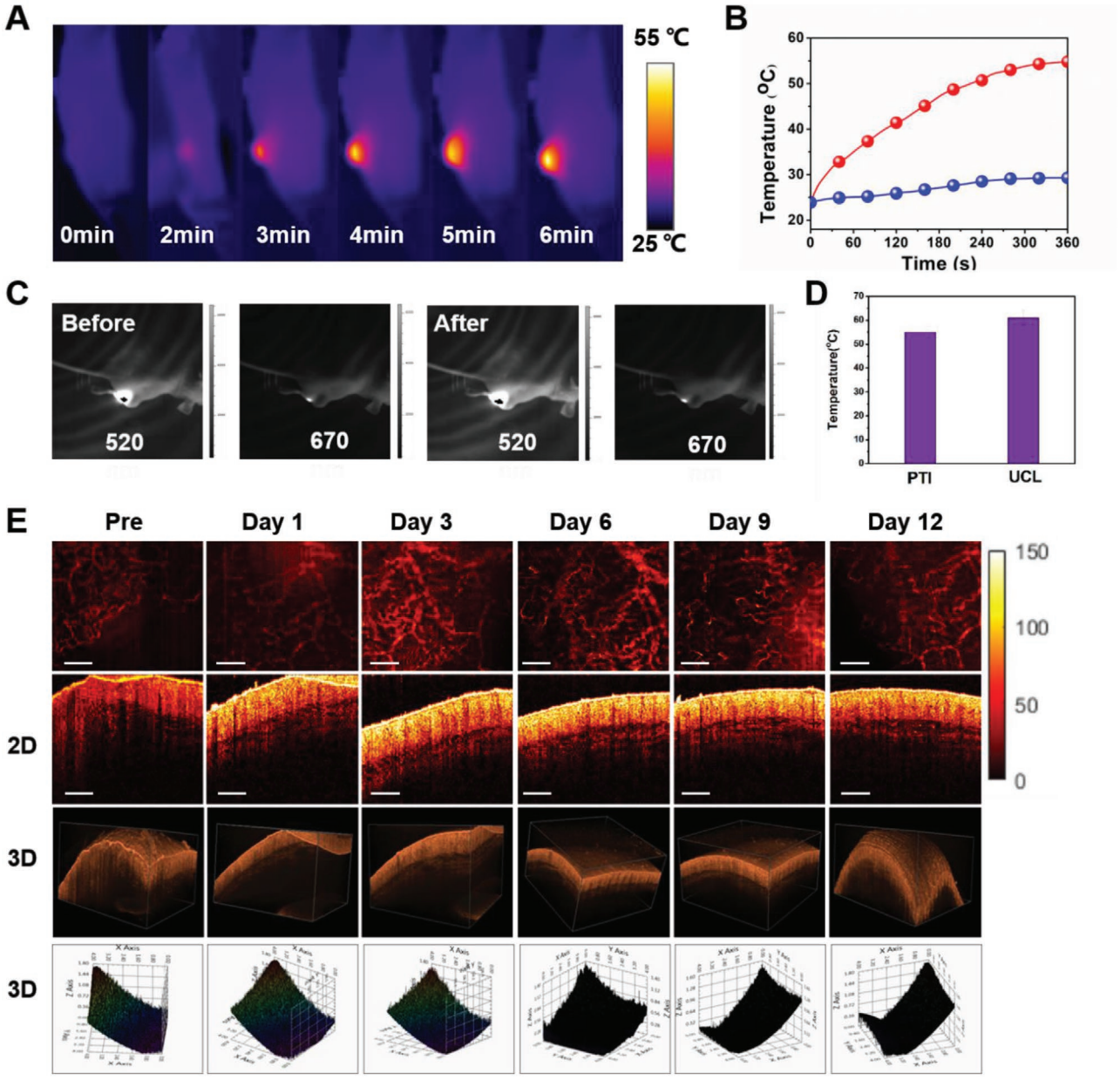

Figure 5. In vivo monitoring of temperature and tumor microenvironments changes in tumor site by using thermal and UCL imaging as well as OCT imaging during PTT. In vivo photothermal images A) and temperature profiles B) of tumors after tail-vein injection of UCILA and PBS upon 1064 nm laser irradiation for 6 min. C) In vivo UCL images of tumor-bearing mice before and after tail-vein injection of UCILA upon 980 nm laser excitation before and after PTT. D) In vivo temperature measured by PTI and UCL spectra after 6 min PTT treatment. E) In vivo OCT angiography in the tumor at different time points of tail-vein injected the UCILA in the form of an averaging window of 3 consecutive B-scans along Y-direction for noise reduction, 2D, 3D, and relative 3D scale bars ($x \times y \times z = 4 \times 4 \times 1.4$ mm), respectively. *All scale bars of the reconstruction images range are 4×4 mm^2.

(Figure 6B), in which high cytotoxicity abilities to A549 cells at all E/T ratios were detected as compared to that from the control group (GFP transfected with unmodified NK-92MI cells). Further analysis indicated that the CAR-NK-92MI cells can specifically kill the B7-H3-positive tumor cells like A549 tumor cells (Figure 6C). Figure 6D exhibited the process of the CAR-NK cells chasing to kill the A549 tumor cells at various coincubation time points. It was discovered that the GFP transfected CAR-NK-92MI cells (the green ones) gradually approached the fusiform A549 cells in the bright field, and then began nibbling the tumor cells at 30 min post coincubation till killed all the A549 cells and left only the green CAR-NK cells at 48 h. More importantly, the Z-stack confocal colocalization images that were captured for GFP transfected CAR-NK-92MI cells coincubated with A549 cells at various incubation time points, offered further evidences of CAR-NK cells targeting to the A549 tumor cells and killing them (Figure S9, Supporting Information). To further investigate the specific killing mechanism of CAR-NK-92MI cells, the expression of CD107a and the secretion of perforin/granzyme B were evaluated by flow cytometry.

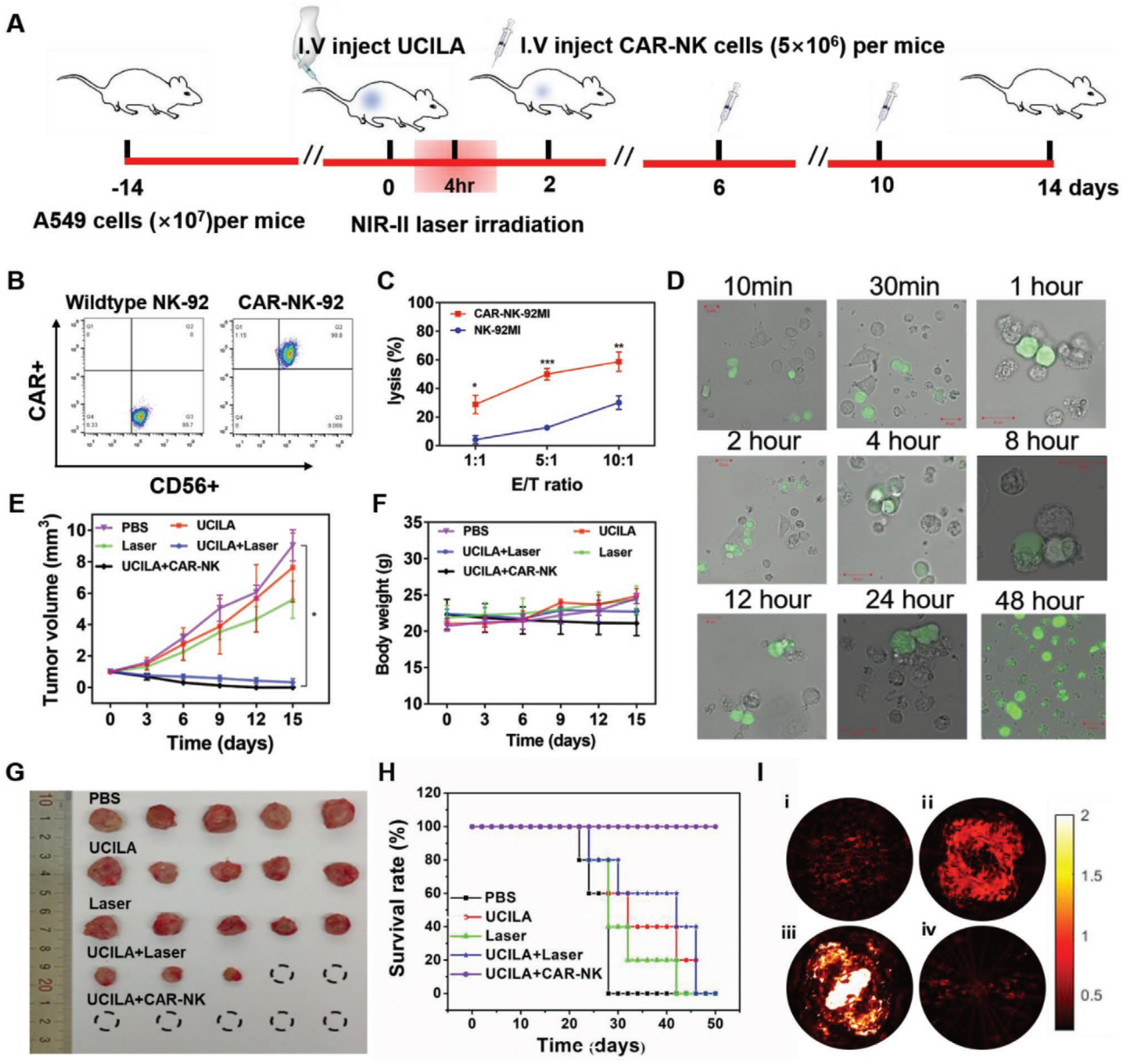

Figure 6. Antitumor efficacy of synergistic temperature-feedback PTT and CAR-NK immunotherapy. A) Schematic illustration of CAR-NK cells further enhancing the efficacy of temperature-feedback PTT. B) Flow cytometric analysis of activated GFP-transfected CAR-NK-92MI cells using CD56 and B7-H3 antibodies. C) Cytotoxicity assay of CAR-NK-92MI cells toward A549 in vitro. D) Confocal images of CAR-NK-92MI cells coincubated with A549 cells at various incubation time (scale bar = 20 μm). E) Tumor volumes variation after treatment with PBS, UCILA, 1064 nm laser, UCILA with 1064 nm laser irradiation and UCILA with 1064 nm laser irradiation followed by CAR-NK immunotherapy, respectively. F) Body weight variation for different treatment groups. G) Photographs of excised tumors from different groups of mice at the end of treatment. H) Optical-resolution photoacoustic microscopy (OR-PAM) images of mice tumor during the treatment. i, ii, iii, and iv denotes the tumor neovasculature at the 7th and 14th day postinoculation of A549 tumor cells and at the 3rd and the 12th day postinjection of UCILA, respectively. *All scale bars of the reconstruction images range are 4×4 mm^2. I) Mice survival curves treated with various groups. *$p < 0.05$, **$p < 0.01$, ***$p < 0.001$.

Figure S10A (Supporting Information) showed that the CD107a expression on surface of CAR-NK-92MI cells was much higher than unmodified NK-92MI. And the levels of perforin and granzyme B were transparently enhanced in CAR-NK-92MI cells in response to the target cell lines (Figure S10B,C, Supporting Information), indicating that CAR-NK-92MI cells exert specific cytotoxicity to A549 cancer cells by elevated secretion of perforin and granzyme B.

Interestingly, it was discovered from Figure 6E that PBS-treated, laser-treated, and UCILA-treated groups showed fast tumor growth. By contrast, the mice in the groups of UCILA with laser and UCILA followed by CAR-NK treatment exhibited inhibited tumor growth with slight body weight change (Figure 6F). In particular, the synergistic treatment demonstrated the capability to eradicate all tumors cells and achieve the best therapeutic efficacy in vivo among other therapeutic

groups (Figure 6G; and Figure S11, Supporting Information). Likewise, the survival curves of tumor-bearing mice also illustrated that the UCILA+Laser+CAR-NK treatment group had the highest average life span over the therapy episode (Figure 6H). Through one-way ANOVA statistical analysis and multiple comparisons of the anticancer data postvarious groups treatments, the results showed that the *p* values derived from UCILA with laser and UCILA with laser and CAR-NK groups versus the PBS group were 0.0238 and 0.0133 respectively, both of which were below 0.05 indicating significant difference. In addition, the *p* values derived from UCILA with laser and CAR-NK group versus the UCILA group was 0.0430, which was below 0.05, indicating that PTT based on UCILA and CAR-NK therapy could exert significant synergetic anticancer effect. Moreover, Figure 6G,H showed that UCILA with laser and CAR-NK treated groups eradicated all the tumors with the highest survival rate and the largest average life span among other groups, which demonstrated the synergetic anticancer effect of precise PTT and CAR-NK immunotherapy.

During the treatment process, the optical-resolution photoacoustic microscopy (OR-PAM), a novel noninvasive and nonionic biomedical imaging method, was utilized to monitor the therapeutic response of tumors at microscale level. Figure 6I shows the representative images of tumors imaged by our optical-resolution photoacoustic microscopy system (OR-PAM) under 532 nm excitation without tail-veil injection of the UCILA nanoparticles, in which the origin of optical-resolution PA contrast is from oxyhemoglobin and hemoglobin in the tumor blood vessels rather than UCILA because the oxyhemoglobin and hemoglobin possess strong absorption at 532 nm, while there is barely absorption of UCILA at this wavelength. And the noninvasive OR-PAM, which is different from aforementioned home-made photoacoustic tomography (PAT, performing in Figure 4) has been used as a supplementary method to monitor the tumor vasculature variation during the therapy process. Image i and ii presented the tumor neovasculature at the 7th and the 14th day postinoculation of the A549 tumor cells, respectively, and the tumor angiogenesis like the growth of the tumor blood vessels was clearly visualized. And the OR-PAM images iii and iv presented the tumor neovasculature at the 3rd and the 12th day post tail-vein injection of the UCILA, respectively, and the blood vessel density of tumor site almost recovered to the normal tissues level, demonstrating the excellent anticancer efficacy of UCILA+CAR-NK strategy in the form of eliminating the tumor neovasculature.

Moreover, the biodistribution and systemic toxicity of UCILA was estimated. After intravenous injection of UCILA, the tumor sites could be gradually visualized within 24 h due to tumor-targeting ability of UCILA (Figure S12A,B, Supporting Information). Mice organs were also collected at 24 h and 14 d postintravenous injection and the concentration of Lu element in these organs was measured by ICP-MS (Figure S12C, Supporting Information). Over time, the concentration of Lu element content in all organs decreased, which indicated the apparent metabolism of UCILA. And the blood biochemical indicators, such as alanine aminotransferase, aspartate aminotransferase, alkaline phosphatase, blood urea nitrogen, etc., have been tested (Figure S13, Supporting Information). All these blood biochemical indicators in the UCILA treated group appears to be normal without meaningful differences compared to the control group, which further highlights the good biosafety of UCILA. Finally, histology analysis was performed to assess the in vivo toxicity of UCILA. Hematoxylin and eosin (H&E) stained images of mice tumor and major organs such as heart, lung, kidney, liver, and spleen that were excised from all the mice after 30 days treatment with PBS or UCILA, were generated. From H&E images (Figure S14, supporting information), it was discovered that the UCILA were mainly distributed inside the tumor areas, causing no damage to normal organs. Consequently, the developed UCILA not only showed excellent penta-modal imaging properties like UCL, PTI, OCT, CT, and PAI in the NIR-II window, but also superior therapeutic efficacy based on cancer-targeting accurate PTT and CAR-NK immunotherapy of lung cancer with fantastic biocompatibility.

3. Conclusion

In this study, a novel NIR-II (≈1000–1700 nm) theranostical nanoplafrom UCILA was constructed, which exhibited both enhanced penta-modal NIR-II imaging ability and favorable NIR-II photothermal therapy at 1064 nm for lung cancer precise detection and treatment. In addition, UCILA as NIR-II laser-irradicated and AS1411-mediated tumor-targeting theranostic agents, also demonstrated high efficacy of synergistic PTT and CAR-NK immunotherapy. Further, this nanotheranostics offered all-round intuitionistic feedbacks from the organism during the whole process of cancer therapy based on the penta-modal imaging. Consequently, it was an efficient way to integrate the aptamer-modified liposome with thermo-sensitive upconversion nanoparticles and the NIR-II organic dye (IR-1048) as a theranostic nanoplatform (UCILA) to acquire omni-directional structural and functional information while exerting cancer-targeting precise photothermal therapy. Because the developed UCILA has been demonstrated that it could not only be fluorescent probe to dynamically monitor the temperature but also could serve as the contrast agent of computed tomography (CT) to real-time track down its metabolization in vivo. Meanwhile, the IR-1048 in UCILA has been proved to be able to serve for both photoacoustic imaging and thermal imaging in the second near-infrared window (NIR-II) besides as PTT agents to heating cancer cells with awesome cytotoxicity and excellent efficacy in vivo. Furthermore, the spherical UCILA enhanced photoacoustic imaging depth up to 4.5 cm and high signal-to-noise ratio at the NIR-II window in the phantom and chick-breast assay. Moreover, UCILA uptaked by A549 cells after 6 h coincubation and showed strong cytotoxicity with photothermal conversion efficiency at 31.3%. Additionally, the positive correlation between fluorescence intensity of UCILA and its photothermal temperature, which realized accurate monitoring to the temperature of photothermal therapy and photothermal imaging. In the tumor-bearing mice model, UCILA not only obviously enhanced the in vivo imaging effects of CT and PAI, but also transparently improved dynamic scattering signals of tumor microvasculature under the NIR-II OCT angiography, manifesting that the UCILA could be hired as contrast agents for CT, PAI, and OCT in the second near-infrared window. After the precise photothermal therapy, the

tumors in the living mice were almost ablated without overheat to the circumambient normal tissue and cells. And the UCILA and CAR-NK cotreated group mice showed no relapse and no metastasis in other organs and acquired well recovery among other groups. Thanks to the complementary guidance of penta-modal imaging, UCILA was proved to be efficient to eliminate the nonsmall-cell lung carcinoma with minimal side-effect. Therefore, we demonstrated that UCILA is an effective strategy to thoroughly remove lung cancer by precise photothermal therapy meanwhile employing penta-modal imaging methods and CAR-NK immunotherapy. And the synergistically combination of five different imaging methods used clinically or preclinically provides all-round intuitionistic feed-back from the organism during the whole process of cancer therapy, in that UCILA is an awesome "one for all" example that evoked each imaging methods supplying their own distinguishing features and characteristics almost all in the second near-infrared window (NIR-II) besides the NIR-II photothermal therapy, which is significant for more precise measurements of therapeutic response to achieve ideal therapeutic effects, and ameliorating patient prognosis.

4. Experimental Section

Materials: IR-1048 was purchased from Sigma-Aldrich, DSPE-PEG_{1k}, DSPE-PEG_{2k} -MAL, DPPC, and cholesterol were purchased from Avanti Polar Lipids Inc., 5'-SH-AS1411 (5'-SH-$(CH_2)_6$-GGT GGT GGT GGT TGT GGT GGT GGT GG-3') was customized by Sangon Biotech (Shanghai) Co., Ltd., $ErCl_3{\cdot}6H_2O$, $YbCl_3{\cdot}6H_2O$, $LuCl_3{\cdot}6H_2O$, 1-octadecene(90%) (ODE) and oleic acid (90%) (OA), were purchased from Sigma-Aldrich, CF_3COONa were purchased from GFS Chemicals, Lu $(CF_3COO)_3$ was prepared by dissolving the Lu_2O_3 in excess CF_3COOH and then evaporating CF_3COOH and water completely. Cell counting Kit-8 (CCK-8) was purchased from Beyotime biotechnology, trypsin was purchased from Gibco USA, Calcein-AM & Propidium Iodide were purchased from Invitrogen USA. All other chemicals were used without further purification. Milli-Q (18.25 MΩ cm, 23 °C, EMD Millipore) was used in all experiments.

Synthesis and Characterization of UCNPs: $NaLuF_4$:Yb/Er@$NaLuF_4$ core–shell nanoparticles were synthesized based on a previously reported procedure with certain modification. $YbCl_3{\bullet}6H_2O$ 0.2 mmol, $YCl_3{\bullet}6H_2O$ 0.78 mmol, and $ErCl_3.6H_2O$ 0.02 mmol were dissolved in 6 mL OA, 15 mL ODE, and the mixtures were heated to 150 °C and kept 30 min, then cool down to room temperature under argon protection. Thus, NH_4F (4 mmol), NaOH (2.5 mmol) were dissolved in 8 mL methanol and added to three-neck flask. Afterward, the solution was heated to 80 °C to remove methanol and subsequently heated to 300 °C for 1 h. After that, 0.15 mmol $NaLuF_4$ inert shell precursor in ODE was injected into reaction mixture and ripened for 10 min. Finally, the solution was cooled down to room temperature and precipitated by ethanol, centrifuged for three times and dispersed in cyclohexane. Next, for phase transfer the UCUPs, 10 mL of 10 mg mL^{-1} UCNPs solution mixed with 10 mL of 0.1 M HCl solution and were stirred for 8 h to obtain the ligand-free UCNPs. After centrifugation (13 500 r min^{-1}, 20 min) twice, the resulted UCNPs were redispersed in 10 mL deionized water. UCNPs were characterized by a Tecnai G2 F20 S-Twin electron microsocopy operating at 200 KV for TEM measurements. X-ray diffraction (XRD) measurements of UCNPs were performed with a Rigaku D/max-2000 diffractometer using Cu Ka radiation (λ = 1.5406 Å). UCL spectra of UCNPs were obtained with Horiba spectrometer upon 980 nm laser irradiation.

Synthesis, Preparation, and Characterization of UCILA: The AS1411 modified liposomes were synthesized by Michael addition reaction between the thiolated ends of AS1411 aptamer (5'-SH-$(CH_2)_6$-GGT GGT GGT GGT TGT GGT GGT GGT GG-3') and maleimide group at the ends of the DSPE-PEG. Briefly, the 5'-SH-AS1411 was pretreated in 90 °C for 5 min to form the G-quadruplex aptamer, then remove the excess DSPE-PEG_{2k}-maleimide by five times of centrifugal (3000 rpm, MWCO 5000) ultrafiltration for 3 min after reaction with the DSPE-PEG-mal overnight at 4 °C, in this way the DSPE-PEG-AS1411 was acquired and the molecular weight was measured by MALDI-TOF-MS. Afterward, UCNPs and IR-1048 coloaded AS1411-liposomes (UCILA) were prepared by film dispersion and membrane extrusion method. Namely, the lipid nanomaterials for UCILA are comprised of DPPC, DSPE-PEG_{1k}, DSPE-PEG-AS1411 and cholesterol with a molar ratio of 10:5:1:1. The lipids and IR-1048 (lipids: IR-1048 = 10:1, w/w) were dissolved in chloroform then dried by a rotary vacuum evaporator to form a uniform film containing hydrophobic IR-1048. Subsequently, the lipid film was hydrated with UCNPs mixed milli-Q. Next, the UCILA solution was freezed for 10 min and thawed for 10 min, which was repeated for five cycles. Then the UCILA solution was extruded through a 100 nm membrane by Avanti Miniextruder. Finally, the UCILA solution was put into dialysis bag (MWCO = 3500) against phosphate buffer saline (PBS, pH = 7.4) and filtered through a 0.22 μm pinhole filter membrane to remove the unencapsulated impurities. The size distribution profile and zeta potential of the UCILA were measured by Zetasizer NanoZS (Malvern, UK) and TEM. It is also characterized by fluorometer and Fourier transform infrared spectroscopy (FT-IR, Perkin Elmer Precise Spectrum 100 Infrared Spectrometer, US). All the measurements of the absorption spectrum were performed on UV–vis 1700 spectrophotometer. Blank liposomes were prepared and characterized by the same procedures.

In Vitro Photothermal Effect of UCILA: The in vitro photothermal effect of different concentrations (5.3, 10.7, 21.4, 42.7, and 85.5 μg mL^{-1}) of UCILA was separately measured upon 1064 nm laser irradiation (1 W cm^{-2}) for 6 min, and the same volume of milli-Q water is a control. The photothermal effect of UCILA (42.75 μg mL^{-1}) at different laser power (0.25, 0.5, 1 W cm^{-2}) for 6 min was also investigated. The temperature was recorded every 10 s by fluke thermal imager. The photothermal stability of UCILA was tested by measuring the periodic heating under 1064 nm laser (1 W cm^{-2}) for 6 min and cooling process of UCILA. The photothermal conversion efficiency (η) of UCILA was calculated by equation previously reported.[31]

Cellular Uptake and In Vitro Photothermal Cytotoxicity: Human nonsmall-cell lung cancer cell A549 cells and mouse fibroblast cell L929 cells were used to evaluate the cellular uptake and in vitro photothermal cytotoxicity of UCILA. The A549 cells were cultured with Dulbecco's modification of Eagle's medium Dulbecco (DMEM)/F12 (1:1, 1 ×, Gibco, USA) including 10% fetal bovine serum (FBS, Gibco, USA) and 1% penicillin-streptomycin (PS, Gibco, USA) in an incubator under 5% CO_2 and constant temperature at 37 °C. And the L929 cells were cultured with RPMI Medium 1640 (1 ×, Gibco, USA) including 15% heat-inactivated fetal bovine serum (FBS, Gibco, USA) and 1% penicillin-streptomycin (PS, Gibco, USA) in an incubator under 5% CO_2 and constant temperature at 37 °C. The human NK-92MI cells were cultured in α minimum essential medium (GIBCO), which supplemented with 0.1×10^{-3} M 2-mercaptoethanol (Sigma-Aldrich), 0.2×10^{-3} M inositol (Sigma-Aldrich), 0.02×10^{-3} M folic acid (Sigma-Aldrich), adjusting to a final concentration of 12.5% horse serum (GIBCO), 12.5% FBS, 100 U mL^{-1} penicillin, and 100 μg mL^{-1} streptomycin. For cellular uptake investigation, the fluorescent tracer- Cy5.5 was used to do the flow cytometry analysis, while for getting rid of the influence of fluorescent dye itself and further comparison of the potential difference, Nile Red was selected to label the UCILA by encapsulation and DAPI was selected to stain the A549 cell nucleus in the laser scanning confocal microscopy. And the Cy5.5-labeled or Nile Red-loaded UCILA (concentration of Cy5.5 or Nile Red at 200 ng mL^{-1}) were incubated in 24-well plates with A549 cells (1×10^5 cells per well) for 2, 4, 6, 12 h, separately. Subsequently, the cells were washed with PBS and centrifuged for 3 min (1000 rpm) then resuspended in PBS to quantify by the flow cytometer and imaged by a laser scanning confocal microscope including the Z-stack images (Carl Zeiss LSCM 710, Germany), respectively. To detect the expression of B7-H3 on the surface of A549 cells, the A549 cells was stained with anti-B7-H3 IgG 8H9 in PBS supplemented with 3% FBS for 30 min at

4 °C. Then cells were rinsed, and further incubated with PE-conjugated goat antihuman IgG secondary antibody (Thermo Fisher Scientific) for another 30 min at 4 °C. Next, the stained cells were analyzed on the AccuriC6 Flow Cytometer (BD Biosciences) after washing. Flow cytometry data were analyzed with FlowJo software.

For the in vitro photothermal cytotoxicity, the logarithmic-phase A549 and L929 cells were seeded into 96-well plates with 1×10^4 cells each well and grown for 12 h, then the mediums were replaced by fresh medium containing 1) PBS, 2) laser, 3) different concentrations of UCILA (with IR-1048 equivalent to 5.3, 10.7, 21.4, 42.7, and 85.5 μg mL^{-1}), and 4) UCILA upon irradiation by 1064 nm the second near-infrared laser for 6 min (1 W cm^{-2}). The relative cell viability was assessed by a standard CCK-8 assay after 24 h coincubation and the absorbance per well was measured under 450 nm with a SpectraMax M5 microplate reader (Molecular Devices, USA). And the Calcein-AM/PI dual-staining experiments were conducted to further evaluate the in vitro therapeutic efficacy of UCILA. And the cytotoxicity of CAR-NK-92MI cells toward A549 cells at the different effector to target (E/T) ratios was evaluated using the Calcein-AM efflux assay. Briefly, A549 cells (5×10^3 cells per well in a 96-well plate) were used as target cells which were labeled with 10 μmol L^{-1} Calcein-AM (Invitrogen) for 30 min at 37 °C, followed by cocultured with effector cells at different E/T ratios of 10:1, 5:1, and 1:1 in total volume of 200 μL for 2 h at 37 °C, respectively. Target tumor cells in the absence of ZsGreen-positive CAR-expressing NK-92MI cells were implemented on detection of spontaneous release. Target cells with the addition of lysis buffer were used for detection of max lysis. 2 h later, cells were further centrifuged and the left supernatants of cell mixture were collected for detection. The fluorescence intensity in the supernatants were measured using a PerkinElmer Victor X3 Microplate Reader (Perkin Elmer, EX 495 nm, EM 515 nm). After the indicated incubation time, the cells were imaged by Carl Zeiss 710 laser scanning confocal microscope.

In Vitro PA Imaging by Phantom and Chicken Breast Assay: The in vitro PAI was used to investigate whether the UCILA could enhance the photoacoustic effects and the imaging depth in biological tissue by phantom and chicken breast tissue. The 200 μL tubes were first filled with different concentrations of UCILA then immersed the tubes into the water. The photoacoustic signals were detected by the home-made PAI system that mainly consists of laser emission system (SURELITE OPO PLUS Optical Parametric Oscillator), rectangular prism, beam expander, rotator, transducer, water tank, amplifier, trigger line, oscilloscope, and computer. The revolving pulsed laser from Nd: YAG (wavelengths: 680–1064 nm) stimulated the phantom or the mice tumor to generate complex wave field signals that were converted to digital signals after amplification by a Pulse/Receiver (5073R, Olympus). Then the photoacoustic images were acquired by reconstruction of delay-sum beam forming algorithm. The solid phantom made up of 1–2% ager solution and intralipid was embedded with different concentrations of UCILA (calculated by IR-1048) or chicken breast of different thickness (1.5, 2.1, 3.0, 4.0, and 4.5 cm) to test their photoacoustic effects and imaging depth.

US-Assisted Photothermal Therapy and CAR-NK Immunotherapy: In vivo photothermal therapy on the mice and all the other animal experiments in vivo were performed according to protocols approved by the Animal Management and Ethics Committee of the University of Macau, whose approval number is UMARE-033-2020. T-cell-deficient male nude (nu/nu) mice (4–5 weeks old) were supplied by the Animal Facility in Faculty of Health Sciences, University of Macau. The human nonsmall-cell lung cancer-bearing mice model were established by subcutaneously injecting A549 cells (5×10^6) in 100 μL PBS to each mouse. Tumor-bearing mice were used for photothermal therapy by tail-vein injections (1.5 mg kg^{-1} per mouse) when the tumor size reach to ≈80–140 mm^3. In order to make the UCILA penetrate deeper into the solid tumors,[46] pulsed ultrasound (1 W cm^{-2}, WELLD ultrasonic treatment apparatus, China) was employed to pretreat the tumor site of all the mice for 3 min. Subsequently, the tumor-bearing mice were randomly divided into five groups ($n = 5$): 1) PBS; 2) UCILA without 1064 nm laser; 3) PBS upon 1064 nm laser irradiation (1 W cm^{-2} for 6 min); 4) UCILA upon 1064 nm laser irradiation Laser (1 W cm^{-2} for 6 min), 5) UCILA upon 1064 nm laser irradiation Laser (1 W cm^{-2} for 6 min) followed by treatments with CAR-NK-92MI cells (5×10^6) for 1 time after 2 days of PTT and continued with the same dose every 4 days, totally for 3-time CAR-NK-92MI treatments. The irradiation was conducted at 4 h postintravenous injection, and then the antitumor effect was evaluated by monitoring the tumor volume and body weight change in each group every 3 days. Tumor volume = (tumor length) × (tumor width)^2/2. The survival rate of each group was calculated after 30 day photothermal therapy. At last, the mice were sacrificed, and their tumors, heart, liver, spleen, lungs, and kidneys were resected for subsequent immunohistochemical analysis stained by H&E.

In Vivo Penta-Modal Imaging (PTI, UCL, PAI, CT, OCT): The in vivo penta-modal imaging including fluorescence imaging, PAI, CT, and OCT were conducted along with the in vivo thermal imaging. For PTI, the temperature of tumor site upon the irradiation of 1064 nm laser was recorded by fluke thermal imager at different time points after intravenous tail-vein injection of UCILA. The in vivo UCL imaging (980 nm laser as excitation source), as well as the UCILA biodistribution in vivo and ex vivo in excised mice tumors, heart, liver, spleen, lungs, and kidneys were imaged by live animal imager (IVIS Lumina, Caliper Life Science). Meanwhile, the in vivo UCL spectra were also recorded by a fiber spectrometer (Ocean Optics FLAME-S-XR1). Those lung cancer-bearing mice were imaged before and after intravenous tail-vein injection of UCILA under 1064 nm laser irradiation at different time points (2, 4, 6, and 12 h) by the home-made multispectral photoacoustic tomography systems (Continuum Surelite I-10; Wavelength: 680–1064 nm; Pulse duration: 5–10 ns; Frequency rate: 20 Hz) and optical-resolution photoacoustic microscopy (532 nm laser as excitation source, OR-PAM, VIS-50). Specifically, a pulsed laser from Nd:YAG laser crystal as the laser source illuminated mice tumors through an optical subsystem with 1064 nm wavelength. A 360° arc rotation olympus-NDT V303-SU transducer (10MHz central frequency; bandwidth range from 0.65 to 1.18 MHz) by a rotary stage was adopted to collect the photoacoustic signals. The emitting complex wave field signals from the mouse tumor were amplified by an Olympus 5073R Pulser/Receiver and then converted into digital signals. Afterward, the photoacoustic images were gained through reconstruction by a delay-and-sum beam forming algorithm. The CT imaging was performed by a preclinical CT System (SuperArgus, Sedecal). The Imaging parameters were set as: 50 KV, 300 μA, 33 μm of resolution, and 39 ms of exposure time. The 3D reconstructed CT images of mice were fulfilled by a mide software (version 1.0.4). It was also explored whether the UCILA could be a contrast agent for CT to real-time track down its metabolization in vivo following in vitro CT imaging of UCILA solution at different concentrations based on the UCNPs. To further optimize the therapeutic strategy based on the tumor vasculatures change, the OCT imaging system was hired (TELESTO-II-1325LR, Thorlabs Inc., USA) to do the in vitro phantom of UCILA and in vivo live mice tumor imaging at 1325 nm. For each measurement, the tail-veil injection of the UCILA was performed to conduct the OCT imaging of mice tumor.

Supporting Information

Supporting Information is available from the Wiley Online Library or from the author.

Acknowledgements

M.X. and B.X. contributed equally to this work. This work was supported by the University of Macau (Nos. MYRG 2020-00067-FHS, MYRG2019-00082-FHS, and MYRG2018-00081-FHS), the Macao Science and Technology Development Fund (Nos. FDCT 0020/2019/AMJ and FDCT 0011/2018/A1), Shenzhen Basic Research Project (No. JCYJ20180305125425815), and Guangdong-Hong Kong-Macao Greater

Bay Area Center for Brain Science and Brain-Inspired Intelligence Fund (No. 2019011).

Conflict of Interest

The authors declare no conflict of interest.

Data Availability Statement

Research data are not shared.

Keywords

CAR-NK, multimodal imaging, photothermal therapy, temperature-feedback, the second near-infrared window

Received: March 9, 2021
Revised: April 6, 2021
Published online: June 23, 2021

[1] H. Sung, J. Ferlay, R. L. Siegel, M. Laversanne, I. Soerjomataram, A. Jemal, F. Bray, *CA Cancer J. Clin.* **2021**, *0*, 1.
[2] R. S. Herbst, D. Morgensztern, C. Boshoff, *Nature* **2018**, *553*, 446.
[3] K. M. Atkins, T. L. Chaunzwa, N. Lamba, D. S. Bitterman, B. Rawal, J. Bredfeldt, C. L. Williams, D. E. Kozono, E. H. Baldini, A. Nohria, U. Hoffmann, H. Aerts, R. H. Mak, *JAMA Oncol.* **2021**, *7*, 206.
[4] G. Kothari, J. Korte, E. J. Lehrer, N. G. Zaorsky, S. Lazarakis, T. Kron, N. Hardcastle, S. Siva, *Radiother. Oncol.* **2021**, *155*, 188.
[5] X. C. Zhang, J. Wang, G. G. Shao, Q. Wang, X. Qu, B. Wang, C. Moy, Y. Fan, Z. Albertyn, X. Huang, J. Zhang, Y. Qiu, S. Platero, M. V. Lorenzi, E. Zudaire, J. Yang, Y. Cheng, L. Xu, Y. L. Wu, *Nat. Commun.* **2019**, *10*, 1772.
[6] S. G. Huang, C. I. Fong, M. Z. Xu, B. N. Han, Z. Yuan, Q. Zhao, *J. Innovative Opt. Health Sci.* **2019**, *12*, 1941002.
[7] J. Chen, X. Tan, S. L. Luo, L. Long, L. Liu, Z. J. Liu, Y. Wang, C. M. Shi, *J. Innovative Opt. Health Sci.* **2018**, *11*, 1850016.
[8] X. J. Men, Z. Yuan, *J Innovative Opt. Health Sci.* **2019**, *12*, 1930001.
[9] H. P. Xu, L. Dong, Z. Bin, Y. S. Huo, S. F. Lin, L. Chang, C. Chen, C. L. Wang, *Drug Delivery* **2020**, *27*, 378.
[10] Y. Zhao, W. Liu, Y. Tian, Z. Yang, X. Wang, Y. Zhang, Y. Tang, S. Zhao, C. Wang, Y. Liu, J. Sun, Z. Teng, S. Wang, G. Lu, *ACS Appl. Mater. Interfaces* **2018**, *10*, 16992.
[11] Y. Zou, Y. P. Sun, B. B. Guo, H. Wei, Y. F. Xia, Z. Y. Huangfu, F. H. Meng, J. C. M. van Hest,, J. D. Yuan, Z. Y. Zhong, *ACS Appl. Mater. Interfaces* **2020**, *12*, 14905.
[12] F. Li, X. Y. Li, Z. M. Li, W. X. Ji, S. Lu, W. L. Xia, *Theranostics* **2020**, *10*, 5528.
[13] M. Karpuz, M. Silindir-Gunay, A. Y. Ozer, S. C. Ozturk, H. Yanik, M. Tuncel, C. Aydin, G. Esendagli, *Eur. J. Pharm. Sci.* **2021**, *156*, 105576.
[14] Y. B. Liu, M. Z. Xu, Y. L. Dai, Q. Zhao, L. P. Zhu, X. W. Guan, G. Li, S. H. Yang, Z. Yuan, *ACS Appl. Polym. Mater.* **2020**, *2*, 1964.
[15] G. G. Yang, Z. Y. Pan, D. Y. Zhang, Q. Cao, L. N. Ji, Z. W. Mao, *ACS Appl. Mater. Interfaces* **2020**, *12*, 43444.
[16] K. W. Chang, Y. B. Liu, D. H. Hu, Q. F. Qi, D. Y. Gao, Y. T. Wang, D. L. Li, X. J. Zhang, H. R. Zheng, Z. H. Sheng, Z. Yuan, *ACS Appl. Mater. Interfaces* **2018**, *10*, 7012.
[17] H. B. Chen, J. Zhang, K. W. Chang, X. J. Men, X. F. Fang, L. B. Zhou, D. L. Li, D. Y. Gao, S. Y. Yin, X. J. Zhang, Z. Yuan, C. F. Wu, *Biomaterials* **2017**, *144*, 42.
[18] T. T. Li, Y. Geng, H. X. Zhang, J. Wang, Y. Feng, Z. Y. Chen, X. X. Xie, X. Qin, S. Li, C. H. Wu, Y. Y. Liu, H. Yang, *Expert Opin. Drug Delivery* **2020**, *17*, 725.
[19] R. An, P. Lei, P. Zhang, X. Xu, J. Feng, H. Zhang, *Nanoscale* **2018**, *10*, 1394.
[20] B. Dong, B. Cao, Y. He, Z. Liu, Z. Li, Z. Feng, *Adv. Mater.* **2012**, *24*, 1987.
[21] X. Li, Z. Yi, Z. Xue, S. Zeng, H. Liu, *Mater. Sci. Eng., C* **2017**, *75*, 510.
[22] Y. J. Liu, P. Bhattarai, Z. F. Dai, X. Y. Chen, *Chem. Soc. Rev.* **2019**, *48*, 2053.
[23] X. Sun, J. Sun, B. Dong, G. Huang, L. Zhang, W. Zhou, J. Lv, X. Zhang, M. Liu, L. Xu, X. Bai, W. Xu, Y. Yang, X. Song, H. Song, *Biomaterials* **2019**, *201*, 42.
[24] X. Liu, Z. Fan, L. Zhang, Z. Jin, D. Yan, Y. Zhang, X. Li, L. Tu, B. Xue, Y. Chang, H. Zhang, X. Kong, *Biomaterials* **2017**, *144*, 73.
[25] L. V. Wang, S. Hu, *Science* **2012**, *335*, 1458.
[26] L. Cheng, S. Shen, S. Shi, Y. Yi, X. Wang, G. Song, K. Yang, G. Liu, T. E. Barnhart, W. Cai, Z. Liu, *Adv. Funct. Mater.* **2016**, *26*, 2185.
[27] L. Du, H. Qin, T. Ma, T. Zhang, D. Xing, *ACS Nano* **2017**, *11*, 8930.
[28] D. Gao, P. Zhang, Y. Liu, Z. Sheng, H. Chen, Z. Yuan, *Nanoscale* **2018**, *10*, 19742.
[29] S. Wang, Y. Xiao, D. D. Zhang, P. K. Wong, *Biomaterials* **2018**, *156*, 56.
[30] L. B. Zhou, Y. Jing, Y. B. Liu, Z. H. Liu, D. Y. Gao, H. B. Chen, W. Y. Song, T. Wang, X. F. Fang, W. P. Qin, Z. Yuan, S. Dai, Z. A. Qiao, C. F. Wu, *Theranostics* **2018**, *8*, 663.
[31] X. Q. Meng, J. L. Zhang, Z. H. Sun, L. H. Zhou, G. J. Deng, S. P. Li, W. J. Li, P. Gong, L. T. Cai, *Theranostics* **2018**, *8*, 6025.
[32] Z. M. Tao, G. S. Hong, C. Shinji, C. X. Chen, S. Diao, A. L. Antaris, B. Zhang, Y. P. Zou, H. J. Dai, *Angew. Chem., Int. Ed.* **2013**, *52*, 13002.
[33] Q. Yang, Z. Hu, S. Zhu, R. Ma, H. Ma, Z. Ma, H. Wan, T. Zhu, Z. Jiang, W. Liu, L. Jiao, H. Sun, Y. Liang, H. Dai, *J. Am. Chem. Soc.* **2018**, *140*, 1715.
[34] S. Lim, H. Y. Yoon, H. J. Jang, S. Song, W. Kim, J. Park, K. E. Lee, S. Jeon, S. Lee, D. K. Lim, B. S. Kim, D. E. Kim, K. Kim, *ACS Nano* **2019**, *13*, 10991.
[35] W. Mu, D. Jiang, S. Mu, S. Liang, Y. Liu, N. Zhang, *ACS Appl. Mater. Interfaces* **2019**, *11*, 23591.
[36] D. F. Chen, W. Yuan, H. C. Park, X. D. Li, *Biomed. Opt. Express* **2020**, *11*, 4316.
[37] M. Farell, A. Self, C. Guza, H. Song, L. Apollon, E. W. Gomez, M. Kumar, *ACS Appl. Mater. Interfaces* **2020**, *12*, 12407.
[38] L. Z. Feng, M. Gao, D. L. Tao, Q. Chen, H. R. Wang, Z. L. Dong, M. W. Chen, Z. Liu, *Adv. Funct. Mater.* **2016**, *26*, 2207.
[39] S. J. Grainger, J. V. Serna, S. Sunny, Y. Zhou, C. X. Deng, M. E. H. El-Sayed, *Mol. Pharmaceut.* **2006**, *7*, 2010.
[40] Y. Huang, E. Hemmer, F. Rosei, F. Vetrone, *J. Phys. Chem. B* **2016**, *120*, 4992.
[41] J. S. Ni, Y. Li, W. Yue, B. Liu, K. Li, *Theranostics* **2020**, *10*, 1923.
[42] A. N. Niemeijer, D. Leung, M. C. Huisman, I. Bahce, O. S. Hoekstra, G. A. M. S. van Dongen, R. Boellaard, S. Du, W. Hayes, R. Smith, A. D. Windhorst, N. H. Hendrikse, A. Poot, D. J. Vugts, E. Thunnissen, P. Morin, D. Lipovsek, D. J. Donnelly, S. J. Bonacorsi, L. M. Velasquez, T. D. de Gruijl, E. F. Smit, A. J. de Langen, *Nat. Commun.* **2018**, *9*, 4664.
[43] M. Ovais, S. Mukherjee, A. Pramanik, D. Das, A. Mukherjee, A. Raza, C. Y. Chen, *Adv. Mater.* **2020**, *32*, e2000055.
[44] P. Si, E. Yuan, O. Liba, Y. Winetraub, S. Yousefi, E. D. SoRelle, D. W. Yecies, R. Dutta, A. de la Zerda, *ACS Nano* **2018**, *12*, 11986.
[45] Q. Sun, Q. You, J. Wang, L. Liu, Y. Wang, Y. Song, Y. Cheng, S. Wang, F. Tan, N. Li, *ACS Appl. Mater. Interfaces* **2018**, *10*, 1963.
[46] S. Lorenzo-Herrero, A. Lopez-Soto, C. Sordo-Bahamonde, A. P. Gonzalez-Rodriguez, M. Vitale, S. Gonzalez, *Cancers* **2018**, *11*, 29.
[47] Y. Fan, P. Wang, Y. Lu, R. Wang, L. Zhou, X. Zheng, X. Li, J. A. Piper, F. Zhang, *Nat. Nanotechnol.* **2018**, *13*, 941.

[48] X. Gao, L. Guo, J. Li, H. E. Thu, Z. Hussain, *J. Controlled Release* **2018**, *292*, 29.
[49] A. Reuben, J. Zhang, S. H. Chiou, R. M. Gittelman, J. Li, W. C. Lee, J. Fujimoto, C. Behrens, X. Liu, F. Wang, K. Quek, C. Wang, F. Kheradmand, R. Chen, C. W. Chow, H. Lin, C. Bernatchez, A. Jalali, X. Hu, C. J. Wu, A. K. Eterovic, E. R. Parra, E. Yusko, R. Emerson, S. Benzeno, M. Vignali, X. Wu, Y. Ye, L. D. Little, C. Gumbs, X. Mao, X. Song, S. Tippen, R. L. Thornton, T. Cascone, A. Snyder, J. A. Wargo, R. Herbst, S. Swisher, H. Kadara, C. Moran, N. Kalhor, J. Zhang, P. Scheet, A. A. Vaporciyan, B. Sepesi, D. L. Gibbons, H. Robins, P. Hwu, J. V. Heymach, P. Sharma, J. P. Allison, V. Baladandayuthapani, J. J. Lee, M. M. Davis, Wistuba, P. A. II Futreal, J. Zhang, *Nat. Commun.* **2020**, *11*, 603.
[50] S. Yang, B. Cao, G. Zhou, L. Zhu, L. Wang, L. Zhang, H. F. Kwok, Z. Zhang, Q. Zhao, *Front. Pharmacol.* **2020**, *11*, 1089.
[51] S. Yang, W. Wei, Q. Zhao, *Int. J. Biol. Sci.* **2020**, *16*, 1767.
[52] D. Zhang, Y. S. Zheng, Z. G. Lin, S. Y. Lan, X. L. Zhang, A. X. Zheng, J. Li, G. Liu, H. H. Yang, X. L. Liu, J. F. Liu, *Small* **2019**, *15*, 1902636.
[53] M. Zhang, W. Yang, P. Wang, Y. Deng, Y. T. Dong, F. F. Liu, R. Huang, P. Zhang, Y. Q. Duan, X. D. Liu, D. Lin, Q. Chu, B. Zhong, *Nat. Commun.* **2020**, *11*, 6119.
[54] X. Zhu, J. Li, X. Qiu, Y. Liu, W. Feng, F. Li, *Nat. Commun.* **2018**, *9*, 2176.
[55] H. S. Jung, P. Verwilst, A. Sharma, J. Shin, J. L. Sessler, J. S. Kim, *Chem. Soc. Rev.* **2018**, *47*, 2280.
[56] D. Wang, B. Xue, J. Song, J. L. Qu, *J. Mater. Chem. C* **2018**, *6*, 6597.
[57] H. Xiang, L. Zhao, L. Yu, H. Chen, C. Wei, Y. Chen, Y. Zhao, *Nat. Commun.* **2021**, *12*, 218.
[58] D. Jaque, L. Martinez Maestro, B. del Rosal, P. Haro-Gonzalez, A. Benayas, J. L. Plaza, E. Martin Rodriguez, J. Garcia Sole, *Nanoscale* **2014**, *6*, 9494.
[59] D. Jaque, F. Vetrone, *Nanoscale* **2012**, *4*, 4301.
[60] L. D. Carlos, F. Palacio, *Thermometry at the Nanoscale: Techniques and Selected Applications*, RSC, Cambridge.
[61] Y. K. Kshetri, C. Regmi, B. Chaudhary, H. S. Kim, T. H. Kim, F. Rosei, S. W. Lee, *J. Lumin.* **2021**, *230*, 117739.
[62] S. S. Zhou, K. M. Deng, X. T. Wei, G. C. Jiang, C. K. Duan, Y. H. Chen, M. Yin, *Opt. Commun.* **2013**, *291*, 138.
[63] L. Marciniak, A. Bednarkiewicz, W. Strek, *J. Lumin.* **2017**, *184*, 179.
[64] E. Carrasco, B. del Rosal, F. Sanz-Rodriguez, A. J. de la Fuente, P. H. Gonzalez, U. Rocha, K. U. Kumar, C. Jacinto, J. G. Sole, D. Jaque, *Adv. Funct. Mater.* **2015**, *25*, 615.
[65] G. Lucchini, A. Speghini, P. Canton, F. Vetrone, M. Quintanilla, *Nanoscale Adv.* **2019**, *1*, 757.
[66] B. del Rosal, E. Carrasco, F. Q. Ren, A. Benayas, F. Vetrone, F. Sanz-Rodriguez, D. L. Ma, A. Juarranz, D. Jaque, *Adv. Funct. Mater.* **2016**, *26*, 6060.
[67] Y. L. Shen, H. D. A. Santos, E. C. Ximendes, J. Lifante, A. Sanz-Portilla, L. Monge, N. Fernandez, I. C. Coria, C. Jacinto, C. D. S. Brites, L. D. Carlos, A. Benayas, M. C. Iglesias-de la Cruz, D. Jaque, *Adv. Funct. Mater.* **2020**, *30*, 2002730.
[68] H. Wang, M. Gauthier, J. R. Kelly, R. J. Miller, M. Xu, W. D. O'Brien, J. J. Cheng, *Angew. Chem., Int. Ed.* **2016**, *55*, 5452.
[69] A. Zandi, M. A. Khayamian, M. Saghafi, S. Shalileh, P. Katebi, S. Assadi, A. Gilani, M. S. Parizi, S. Vanaei, M. R. Esmailinejad, F. Abbasvandi, P. Hoseinpour, M. Abdolahad, *Adv. Healthcare Mater.* **2019**, *8*, 1900613.
[70] L. Zhang, H. J. Yi, J. Song, J. Huang, K. Yang, B. Tan, D. Wang, N. L. Yang, Z. G. Wang, X. S. Li, *ACS Appl. Mater. Interfaces* **2019**, *11*, 9355.
[71] L. L. Zhu, H. Y. Zhao, Z. Y. Zhou, Y. H. Xia, Z. G. Wang, H. T. Ran, P. Li, J. L. Ren, *Nano Lett.* **2018**, *18*, 1831.